Available online at www.sciencedirect.com
SCIENCE DIRECT®
ELSEVIER
Computers and Mathematics with Applications 52 (2006) 651–670
An International Journal
computers & mathematics
with applications
www.elsevier.com/locate/camwa

Thermal Characteristics of Mixed Electroosmotic and Pressure-Driven Microflows

P. DUTTA* AND KEISUKE HORIUCHI
Mechanical and Materials Engineering
Washington State University
Pullman, WA 99164-2920, U.S.A.
dutta@mail.wsu.edu

HONG-MING YIN
Department of Mathematics
Washington State University
Pullman, WA 99164-3113, U.S.A.

Abstract—Analytical solutions for the temperature distribution, heat transfer coefficient, and Nusselt number of steady electroosmotic flows with an arbitrary pressure gradient are obtained for two-dimensional straight microchannels. The thermal analysis considers *interaction among advective, diffusive, and Joule heating terms in order to obtain the thermally developing behavior of mixed electroosmotic and pressure-driven flows* with isothermal boundary conditions. Heat transfer characteristics are obtained for low Reynolds number microflows where the viscous and electric field terms are very dominant. The electroosmotic component of the flow velocity is modelled with Helmholtz-Smoluchowski slip velocity, and the mixed flow velocity is presented as linear superposition of pure electroosmotic velocity and plane Poiseuille velocity. In mixed flow cases, the governing equation for energy is not separable in general. Therefore, we introduced *a method that considers the extended Graetz problem.* Analytical results show that the heat transfer coefficient of mixed electroosmotic and pressure-driven flow is smaller than that of pure electroosmotic flow. For the parameter range studied here (Re < 0.7), the fully developed Nusselt number is independent of the thermal Peclet number for both pure electroosmotic and mixed electroosmotic-pressure driven microflows. In mixed electroosmotic and pressure-driven flows, the thermal entrance length increases with the imposed pressure gradient.

Keywords—Microfluidics, Electroosmosis, Joule heating, Heat transfer, Extended Graetz problem.

1. INTRODUCTION

The emerging lab-on-a-chip microfluidic devices are getting more attention in medical, pharmaceutical, and defense applications due to their low cost, less operation time, light weight, and small size. The basic goal of this device is to miniaturize laboratory experiments and all its capabilities to the microscopic level. One of the key functionalities of these "lab-on-a-chip" devices

*Author to whom all correspondence should be addressed.
This work has been funded partially by Washington State University Office of Research and partially by the National Science Foundation (CTS 0300802).

0898-1221/06/$ - see front matter Typeset by AMS-TEX
doi:10.1016/j.camwa.2006.10.002

is to transport liquid or reagent from one place to another. Due to tiny size of these devices, the pumping method needed in these microdevices is quite different from that of macroscale devices. In order to meet the pumping requirements of these "lab-on-a-chip" devices, a number of non-mechanical micropumping techniques, such as electrohydrodynamic, magnetohydrodynamic, and electrokinetic, are under development. Among possible options, the electrohydrodynamic [1] and magnetohydrodynamic [2] pumping require ultra low and ultra high conductive fluid, respectively. Hence, these pumping mechanisms cannot be applied for the biological molecules. A recent study shows that electrokinetic pumping is applicable to a wide range of conductivity of fluids [3]. In electrokinetic pumping an ionized liquid is transported under the action of an externally applied electric field. This mechanism is also known as electroosmosis.

The electroosmosis was first discovered by F.F. Reuss in 1809 from an experimental study on clay diaphragms. This was followed later by the seminal work of Helmholtz (1879) on the electric double layer theory, which relates the electrical and flow parameters for electroosmotic transport. Since the discovery of the electrokinetic phenomenon, there have been numerous analytical, experimental, and numerical studies on this phenomenon. However, so far, most of the studies have focused on the fluid flow behavior under steady [4,5] and unsteady [6–8] electric fields with uniform wall electrochemical conditions, and not much attention has been paid on the thermal behavior.

Since the electroosmotic flow is driven in the presence of a large external electric field, the interaction of the electric field and the charged ions results in thermal energy generation as Joule heating. In typical electroosmotic flows with a fluid of $300\,\mu$ S/m electrical conductivity and an applied electric field of 100 V/mm [9], the Joule heating term contributes $3 \times 10^6\,\mathrm{W/m^3}$. This thermal energy generation and the associated dissipation mechanisms have received very little attention. Lately Maynes and Webb have presented thermal behavior of fully developed combined pressure and electroosmotically driven microflows [10]. Although they considered Joule heating, their analysis is valid only in the fully developed region. In a relatively similar study, Sparrow and coworkers have presented temperature distribution in both developing and the fully developed region for both constant surface temperature and constant heat flux boundary conditions with an arbitrary generation term [11]. That study was based on a high value of thermal Peclet number, and hence they omitted the axial conduction term from the energy equation. In a seminal work, Agrawal has introduced the extended Graetz problem, an analytical technique, to solve the energy equation in the thermally developing region by considering the axial conduction term [12].

In this article, we obtain analytical solutions for temperature distributions and heat transfer characteristics of mixed electroosmotic and pressure-driven flows in two-dimensional microchannels. Both developing and fully developed regions have been analyzed for isothermal channel wall condition. We have utilized separation of variables technique for homogeneous energy equation introduced by Lahjomri and Oubarra, where they solved the thermal problem for arbitrary velocity distribution without any heat generation [13]. Our analysis takes care of interaction among advective, viscous, and Joule heating terms to obtain the temperature distribution within the fluid. This analysis especially identifies the effects of Joule heating in microchannels during electroosmotic and mixed electroosmotic-pressure driven pumping.

2. MATHEMATICAL MODEL

2.1. Electric Double Layer and Electroosmotic Microflow

Electric double layer (EDL) and electroosmotic flows have been discussed extensively in the past [14–16]. In this study, we only review the necessary parameters and governing equations for the complete understanding of the electroosmotic and mixed electroosmotic-pressure driven flows. Figure 1 shows the formation of EDL and electroosmotic flow in a straight microchannel whose walls contain net negative charges. The net (negative) charges on the surface originate from ionization, ion adsorption, or ion dissolution between channel surface and polar working

medium. For example, a fused silica surface attains negative charges in contact with high pH buffer [17]. Due to the presence of net charges on the surface, counter (positive) ions in the fluid get attracted to the wall and coions get repelled from the wall forming an EDL close to the surface. In the EDL the ion concentration of counterions is higher than coions, but outside the EDL both coions and counterions have the same concentration. The EDL is generally estimated in terms of Debye length (λ), and its value depends on the ion concentration of the solution. For example, ion concentrations of 1 mM and 100 mM correspond to Debye length thickness of 10 nm and 1 nm, respectively. Although EDL is formed in most internal flows, its influence is very significant once the channel size is scaled down to micron and submicron level. Electroosmotic pumping is originated when EDL interacts with an external electric field [15]. Since the EDL has net positive charges for the case presented in Figure 1, the streamwise component of the external electric field creates a net movement of positive ions from anode to cathode. Due to the viscous drag, the fluid in the microchannel is pulled by the ions. The steady electroosmotic flow is governed by the modified Navier-Stokes equations as [15]

$$\rho_f \left(\vec{V} \cdot \nabla\right) \vec{V} - \mu \nabla^2 \vec{V} + \nabla P - \rho_e \vec{E} = 0, \tag{1}$$

where ρ_f is the fluid density, μ is the dynamic viscosity, P is the pressure, $\vec{E}$ is the applied electric field, and $\vec{V} = (u, v)$ is the velocity field. The incompressibility condition requires a divergence-free velocity field ($\nabla \cdot \vec{V} = 0$). The first and second terms of equation (1) indicate the inertia and viscous forces, respectively. The third term is due to the pressure gradient in the system, while the final term, $\rho_e \vec{E}$, represents electrokinetic body force due to the formation of the EDL next to the surface. Here ρ_e is the electric charge density, and for a *symmetric dilute electrolyte* it can be found as [15]

$$\rho_e = -2 n_o e z \sinh\left(\frac{ez\psi}{k_B T}\right), \tag{2}$$

where ψ is the electrokinetic potential, n_o is the average number of positive or negative ions in the buffer, e is the electron charge, z is the valence, k_B is the Boltzmann constant, and T is the absolute temperature. At steady state, the electrokinetic potential, ψ, can be obtained from the Poisson-Boltzmann equation as [14]

$$\nabla^2 \psi = -\frac{\rho_e}{\varepsilon}, \tag{3}$$

where ε is the permittivity of the medium.

The main simplifying assumptions and approximations used in forming above equations are:

1. The fluid viscosity is *independent of the shear rate.* Hence, we assume a Newtonian fluid.
2. The fluid viscosity is *independent of the local electric field strength.*
3. Fluid properties are independent of temperature change. This can be justified for smaller temperature change (less than 10 K).
4. The ions are point charges and their convection effects are negligible.
5. The solvent is continuous and its permittivity is not affected by the overall and the local electric field strength.

2.2. Flow Analysis in Two-Dimensional Straight Microchannel

Here we consider that the channel half height, D, is much smaller than the channel width W ($D \ll W$). Therefore, the flow can be treated as two-dimensional or planar as shown in Figure 1. In microfluidic channels, *the flow Reynolds number is very small (*$\mathrm{Re} \ll 1$*) due to smaller length scale and flow velocity*, especially for electroosmotic flows. Hence, the contribution of inertial term is negligible, and we can assume that the flow is hydrodynamically fully developed from the very beginning of the channel. Moreover, in pure electroosmotic microflows there is no pressure

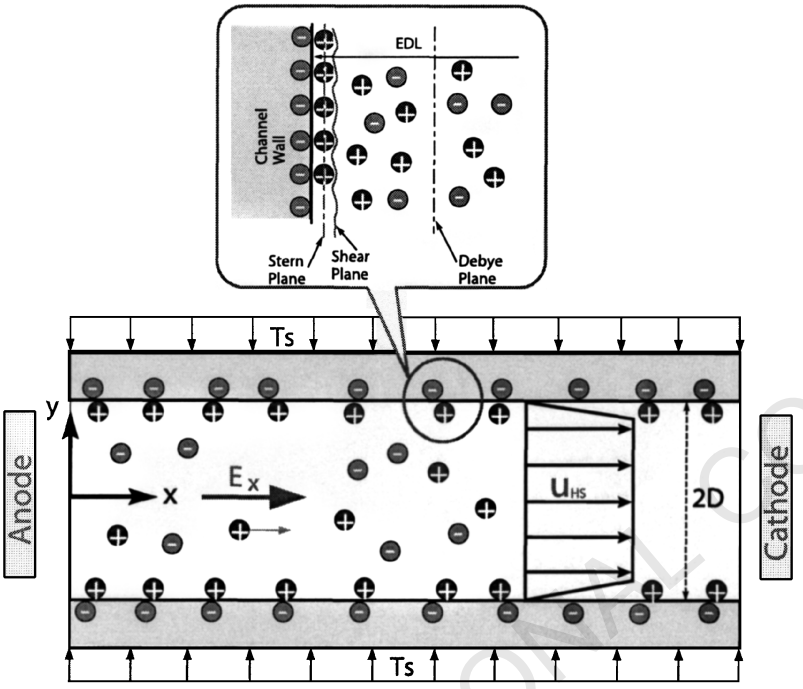

Figure 1. Schematic view of electroosmotically driven flows in a two-dimensional straight channel. Positive charge dominant EDL is formed next to the negatively charged dielectric surfaces. Electroosmotic pumping takes place from the left to right direction due to the interaction of EDL with the externally applied electric field.

gradient in the flow. In the absence of inertial and pressure force terms, the electrokinetic body force term is counterbalanced by the viscous force, and the resulting velocity becomes [15]

$$u(y) = u_{\mathrm{HS}} \left(1 - \frac{\psi}{\zeta}\right), \tag{4}$$

where ζ is the potential at the shear plane, $u_{\mathrm{HS}} = -\zeta \varepsilon E_x/\mu$ is the Helmholtz-Smoluchowski velocity. For a straight microchannel with infinitesimal EDL ($\lambda \ll D$), the steady electrokinetic potential distribution can be found from equation (2) as [5]

$$\psi(y) = \frac{4k_BT}{ez} \tanh^{-1}\left[\tanh\left(\frac{ez\zeta}{4k_BT}\right) \exp\left(\frac{|y| - D}{\lambda}\right)\right]. \tag{5}$$

In the above analysis the zeta potential (ζ), buffer concentration, and electric field strength (E_x) are assumed constant along the channel.

Figure 2 shows the electrokinetic potential (ψ) distribution close to the wall for a working fluid of concentration 1 mM. Here the microchannel thickness is 20 microns and the estimated Debye length is 10 nm. Four different zeta potential values are considered based on recent experimental results [9]. From Figure 2, it is clear that the electrokinetic potential decreases abruptly very close to the wall, and the electrokinetic potential reaches to zero within 5λ from the channel surface. In other words, for a 20 micron thick channel the electroosmotic velocity changes take place within 0.5% of the microchannel if the buffer concentration is 1 mM. Hence, *for infinitesimal EDL, we can neglect the velocity distribution within the EDL, and "plug-like" velocity is justified across the channel.* However, in many practical applications, the pressure gradient originates due to a number of reasons, such as the presence of alternative pumping mechanism or placement of mechanical valve in the flow path. The resulting pressure gradient distorts the plug-like velocity

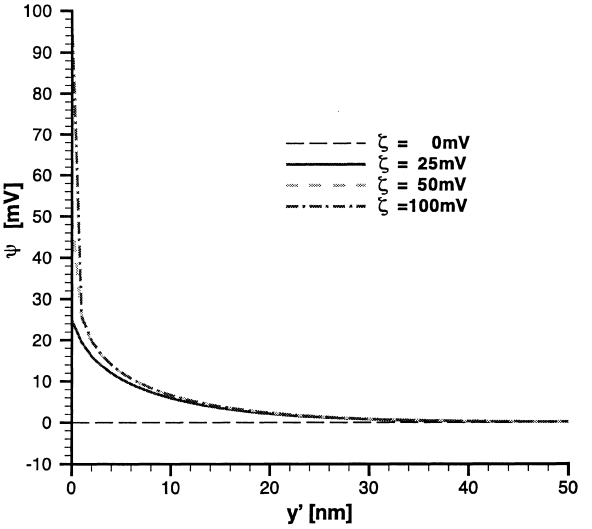

Figure 2. Electrokinetic potential distribution near the wall for different zeta potentials. The channel thickness and Debye length are 20 microns and 10 nm, respectively. Here y' is the distance from the wall.

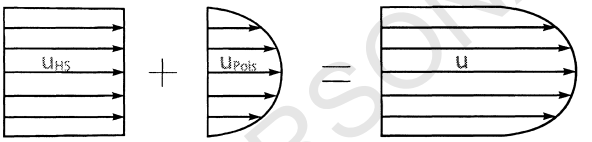

(a) Favorable pressure gradient.

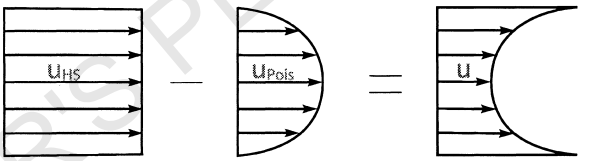

(b) Adverse pressure gradient.

Figure 3. Schematic view of mixed electroosmotic and pressure-driven flows. Under ideal conditions of uniform zeta potential and electrolyte concentration, we obtain pure electroosmotically driven plug flows.

distribution as shown in Figure 3. In the absence of inertial term (Re $\ll$ 1), the momentum equation becomes linear. Therefore, the steady velocity distribution for the mixed electroosmotic and pressure-driven flow in a two-dimensional straight channel can be obtained by considering linear superposition of electroosmotic velocity (u_{EOF}) and plane Poiseuille flow velocity (u_{Pois}) as [5].

$$u(x,y) = u_{\mathrm{EOF}} + u_{\mathrm{Pois}} \cong u_{\mathrm{HS}} - \frac{D^2}{2\mu}\frac{dP}{dx}\left\{1 - \left(\frac{y}{D}\right)^2\right\}. \tag{6}$$

The qualitative velocity profiles are shown in Figure 3 for favorable and adverse pressure gradient flows.

2.3. Energy Transport in Mixed Electroosmotic-Pressure Driven Flows

For steady microflow, the governing equation for thermal energy transport can be presented as

$$\rho_f c_P \left(\vec{V}\cdot\nabla\right) T - \nabla\cdot(k\nabla T) - \Phi - \sigma\left(\vec{E}\cdot\vec{E}\right) = 0, \tag{7}$$

where c_P is the specific heat capacity, k is the thermal conductivity, Φ is the viscous dissipation, and σ is the electrical conductivity of the buffer fluid. The first and second terms of equation (7) indicate the thermal energy transfer due to advection and thermal diffusion, respectively. On the other hand, the third and fourth terms show thermal energy generation in the system due to viscous dissipation and Joule heating, respectively. In microflows, the contribution of viscous dissipation term is much smaller than that of Joule heating term [23]. Hence we neglect the viscous dissipation term for this analysis.

For the isothermal surface thermal case, the two-dimensional energy equation is subjected to the following boundary conditions.

$$T = T_e, \qquad \text{at } x = 0, \quad 0 \le y \le D, \tag{8}$$

$$T < \infty, \qquad \text{at } x \to \infty, \quad 0 \le y \le D, \tag{9}$$

$$\frac{\partial T}{\partial y} = 0, \qquad \text{at } y = 0, \quad 0 \le x < \infty, \tag{10}$$

$$T = T_s, \qquad \text{at } y = D, \quad 0 \le x < \infty, \tag{11}$$

where T_e and T_s are the inlet and surface temperature, respectively.

2.4. Normalization Scheme

We normalize streamwise and cross-stream coordinates (x, y) with the half channel height D ($\xi = x/D$, $\eta = y/D$). Here, D is used as the characteristic length as opposed to hydraulic diameter, D_H ($D_H = 4D$). Hence, the flow Reynolds and Nusselt numbers in this study will be one-fourth of their conventional values where those numbers are calculated based on hydraulic diameter. For convenience, we normalize the flow velocity by Helmholtz-Smoluchowski velocity, u_{HS}. Under this normalization scheme, the nondimensional streamwise velocity becomes

$$U(\eta) = 1 + \Omega\left(1 - \eta^2\right), \tag{12}$$

where Ω is the normalized pressure gradient ($\Omega = -(1/2)\frac{dP^*}{d\xi}$) and P^* is the nondimensional pressure ($P^* = PD/\mu u_{\mathrm{HS}}$). The corresponding mean velocity can be presented as

$$U_m = \frac{1}{A_c}\int_{A_c} U\, dA = \int_0^1 U\, d\eta = 1 + \frac{2}{3}\Omega, \tag{13}$$

where A_c is the cross-sectional area of the channel ($A_c = 2WD$). If we present the normalized temperature as $\theta = (T - T_s)/(T_e - T_s)$, the nondimensional energy equation becomes

$$\mathrm{Pe}_T\, U\frac{\partial \theta}{\partial \xi} = \frac{\partial^2 \theta}{\partial \xi^2} + \frac{\partial^2 \theta}{\partial \eta^2} + G, \qquad \text{in } 0 < \xi < \infty, \quad 0 < \eta < 1, \tag{14}$$

where Pe_T is the thermal Peclet number and G is the normalized Joule heating term. The thermal Peclet number can be found by multiplying flow Reynolds number (Re) with the fluid Prándtl number (Pr), and the normalized source term can be presented as

$$G = \frac{\sigma\left(\vec{E}\cdot\vec{E}\right)D^2}{k(T_e - T_s)}. \tag{15}$$

Therefore, the normalized source term represents a ratio of energy generation to thermal conduction. An aqueous solution (with Tris-EDTA buffer) of conductivity, $\sigma = 90\,\mu\mathrm{S/cm}$ [8], and an applied electric field of $400\,\mathrm{V/mm}$ will contribute to $G = 1$ in a $100\,\mu\mathrm{m}$ thick microchannel for $T_e - T_s = 5K$. In the above normalization process, temperature independence of fluid properties is assumed. Although the fluid viscosity, μ, and thermal conductivity, k, are strong functions of

the fluid temperature, their variation can be neglected for a temperature difference of 10 K or smaller. Moreover, the electrical conductivity (σ) is assumed uniform throughout the channel.

The normalized energy equation presented by equation (14) is a second-order partial differential equation. In order to obtain the temperature solution within the fluid, boundary conditions, equations (8)–(11), also need to be normalized as

$$\theta = 1, \qquad \text{at } \xi = 0, \quad 0 \le \eta \le 1, \tag{16}$$

$$\theta < \infty, \qquad \text{at } \xi \to \infty, \quad 0 \le \eta \le 1, \tag{17}$$

$$\frac{\partial \theta}{\partial \eta} = 0, \qquad \text{at } \eta = 0, \quad 0 \le \xi < \infty, \tag{18}$$

$$\theta = 0, \qquad \text{at } \eta = 1, \quad 0 \le \xi < \infty. \tag{19}$$

3. ANALYSIS OF NORMALIZED ENERGY EQUATION

Let us decompose the normalized temperature, θ, into two parts

$$\theta = \theta_p + \theta_g, \tag{20}$$

where θ_p is chosen such that $\theta - \theta_p$ satisfies a homogeneous equation. Now we seek a particular type of function θ_p as a function of η, $\theta_p = F(\eta)$, subject to the boundary conditions, equations (18) and (19). The resulting governing equation for $F(\eta)$ becomes

$$\frac{d^2F}{d\eta^2} = -G, \qquad \text{in } 0 < \eta < 1, \tag{21}$$

and the corresponding boundary conditions

$$\frac{dF}{d\eta} = 0, \qquad \text{at } \eta = 0, \tag{22}$$

$$F = 0, \qquad \text{at } \eta = 1. \tag{23}$$

By solving equation (21) with the corresponding boundary conditions (equations (22) and (23)), we obtain a solution for particular type of function as

$$\theta_p = F(\eta) = \frac{G}{2}\left(1 - \eta^2\right). \tag{24}$$

Since θ_g is the homogeneous part of the temperature (θ), the governing equation for θ_g can be written as

$$\mathrm{Pe}_T\, U \frac{\partial \theta_g}{\partial \xi} = \frac{\partial^2 \theta_g}{\partial \xi^2} + \frac{\partial^2 \theta_g}{\partial \eta^2}, \qquad \text{in } 0 < \xi < \infty, \quad 0 < \eta < 1, \tag{25}$$

and the corresponding boundary conditions become

$$\theta_g = 1 - \frac{G}{2}\left(1 - \eta^2\right), \qquad \text{at } \xi = 0, \quad 0 \le \eta \le 1, \tag{26}$$

$$\theta_g < \infty, \qquad \text{at } \xi \to \infty, \quad 0 \le \eta \le 1, \tag{27}$$

$$\frac{\partial \theta_g}{\partial \eta} = 0, \qquad \text{at } \eta = 0, \quad 0 \le \xi < \infty, \tag{28}$$

$$\theta_g = 0, \qquad \text{at } \eta = 1, \quad 0 \le \xi < \infty. \tag{29}$$

Suppose the solution to the partial differential equation (25) has the following form (for details see [13]):

$$\theta_g = \sum_{n=1}^{\infty} A_n f_n(\eta) \exp\left[-\frac{\lambda_n^2}{\mathrm{Pe}_T}\xi\right], \qquad \text{in } 0 < \xi < \infty, \quad 0 < \eta < 1, \tag{30}$$

where A_n are the coefficients, f_n are the eigenfunctions, and λ_n are the eigenvalues. Substituting equation (30) into equations (25)–(29), we obtain the following nonlinear eigenvalue problem:

$$\frac{d^2 f_n}{d\eta^2} + \lambda_n^2 \left\{ \left(\frac{\lambda_n}{\mathrm{Pe}_T}\right)^2 + U \right\} f_n = 0, \qquad \text{in } 0 < \eta < 1, \tag{31}$$

$$\frac{df_n}{d\eta} = 0, \qquad \text{at } \eta = 0, \tag{32}$$

$$f_n = 0, \qquad \text{at } \eta = 1. \tag{33}$$

The solution of equation (31) under symmetric boundary condition, equation (32), can be expressed as

$$f_n = \exp\left[-\frac{1}{2}\lambda_n \sqrt{\Omega}\eta^2\right] \, {}_1F_1(a; b; z), \tag{34}$$

where ${}_1F_1(a; b; z) = \sum_{J=0}^{\infty}((a)_J/(b)_J)(z^J/J!)$ is the Kummer confluent hypergeometric function, and

$$a = \frac{-\lambda_n^3 - \mathrm{Pe}_T^2\left(\lambda_n(1+\Omega) - \sqrt{\Omega}\right)}{4\sqrt{\Omega}\,\mathrm{Pe}_T^2},$$

$$b = \frac{1}{2},$$

$$z = \lambda_n \sqrt{\Omega}\eta^2.$$

Here $(a)_J$ and $(b)_J$ are known as Pochhammer symbols [19].

The eigenfunctions $\{f_n\}$ presented by equation (34) have a sequence of eigenvalues $\{\lambda_n\}$, and $\{f_n\}_{n=1}^{\infty}$ forms a base for the function space $L^2(0,1)$. Our next goal is to find the eigenvalues $\{\lambda_n\}$ from equation (34) by utilizing the wall boundary condition given in equation (33). For this nonlinear eigenvalue problem, the secant method is utilized to find out corresponding eigenvalues, and they are presented in Table 1. Note that eigenfunctions $\{f_n\}$ are not mutually orthogonal (by referring to the standard Sturm-Liouville problem) since the eigenvalues $\{\lambda_n\}$ occur nonlinearly in equation (31). We use the Gram-Schmidt orthogonal procedure in order to determine coefficients, $\{A_n\}$, from a set of linearly independent eigenfunctions $\{f_n\}_{n=1}^{\infty}$ [20]. Details of the Gram-Schmidt orthogonal procedure are shown in the Appendix.

From equations (20), (24), and (30), the total solution for the nondimensional temperature becomes

$$\theta = \theta_p + \theta_g = \frac{G}{2}\left(1 - \eta^2\right) + \sum_{n=1}^{\infty} A_n f_n \exp\left[-\frac{\lambda_n^2}{\mathrm{Pe}_T}\xi\right], \tag{35}$$

where λ_n and f_n can be found from equations (33) and (34), and A_n can be found from equations (A.12)–(A.14) (for details see the Appendix). It is important to note that the normalized temperature distribution obtained in equation (35) is valid for $\Omega > -1.5$. As the normalized pressure gradient is less than -1.5, the net flow changes direction, which is undesirable for the presented mathematical model.

Table 1. First 20 terms of eigenvalues (λ_n) and corresponding coefficients (A_n) for $\mathrm{Pe}_T = 5$.

	$\Omega = -1$		$\Omega = 1$		$\Omega = 5$	
n	λ_n	A_n	λ_n	A_n	λ_n	A_n
1	1.869	$+1.3 \times 10^{0} - 5.1 \times 10^{-1}\mathrm{G}$	1.133	$+1.2 \times 10^{0} - 5.2 \times 10^{-1}\mathrm{G}$	0.677	$+1.2 \times 10^{0} - 5.2 \times 10^{-1}\mathrm{G}$
2	4.095	$-4.4 \times 10^{-1} + 1.3 \times 10^{-2}\mathrm{G}$	3.245	$-3.9 \times 10^{-1} + 2.3 \times 10^{-2}\mathrm{G}$	2.188	$-3.4 \times 10^{-1} + 2.8 \times 10^{-2}\mathrm{G}$
3	5.646	$+2.6 \times 10^{-1} - 2. \times 10^{-3}\mathrm{G}$	4.858	$+2.4 \times 10^{-1} - 3.3 \times 10^{-3}\mathrm{G}$	3.576	$+1.8 \times 10^{-1} + 2.5 \times 10^{-3}\mathrm{G}$
4	6.879	$-1.8 \times 10^{-1} + 1.0 \times 10^{-3}\mathrm{G}$	6.162	$-1.7 \times 10^{-1} + 1.0 \times 10^{-3}\mathrm{G}$	4.822	$-1.2 \times 10^{-1} - 6.0 \times 10^{-3}\mathrm{G}$
5	7.930	$+1.4 \times 10^{-1} - 5.3 \times 10^{-4}\mathrm{G}$	7.272	$+1.4 \times 10^{-1} - 4.9 \times 10^{-4}\mathrm{G}$	5.938	$+9.1 \times 10^{-2} + 4.9 \times 10^{-3}\mathrm{G}$
6	8.859	$-1.2 \times 10^{-1} + 3.1 \times 10^{-4}\mathrm{G}$	8.250	$-1.1 \times 10^{-1} + 2.9 \times 10^{-4}\mathrm{G}$	6.947	$-8.0 \times 10^{-2} - 3.3 \times 10^{-3}\mathrm{G}$
7	9.702	$+9.8 \times 10^{-2} - 1.9 \times 10^{-4}\mathrm{G}$	9.133	$+9.7 \times 10^{-2} - 1.9 \times 10^{-4}\mathrm{G}$	7.869	$+7.3 \times 10^{-2} + 2.0 \times 10^{-3}\mathrm{G}$
8	10.478	$-8.5 \times 10^{-2} + 1.3 \times 10^{-4}\mathrm{G}$	9.942	$-8.4 \times 10^{-2} + 1.3 \times 10^{-4}\mathrm{G}$	8.720	$-6.8 \times 10^{-2} - 1.2 \times 10^{-3}\mathrm{G}$
9	11.201	$+7.5 \times 10^{-2} - 9.1 \times 10^{-5}\mathrm{G}$	10.693	$+7.5 \times 10^{-2} - 9.2 \times 10^{-5}\mathrm{G}$	9.511	$+6.3 \times 10^{-2} + 7.5 \times 10^{-4}\mathrm{G}$
10	11.880	$-6.7 \times 10^{-2} + 6.6 \times 10^{-5}\mathrm{G}$	11.396	$-6.7 \times 10^{-2} + 6.7 \times 10^{-5}\mathrm{G}$	10.253	$-5.9 \times 10^{-2} - 4.6 \times 10^{-4}\mathrm{G}$
11	12.523	$+6.0 \times 10^{-2} - 4.9 \times 10^{-5}\mathrm{G}$	12.060	$+6.1 \times 10^{-2} - 5.1 \times 10^{-5}\mathrm{G}$	10.953	$+5.5 \times 10^{-2} + 2.9 \times 10^{-4}\mathrm{G}$
12	13.134	$-5.5 \times 10^{-2} + 3.8 \times 10^{-5}\mathrm{G}$	12.690	$-5.5 \times 10^{-2} + 3.9 \times 10^{-5}\mathrm{G}$	11.616	$-5.1 \times 10^{-2} - 1.9 \times 10^{-4}\mathrm{G}$
13	13.719	$+5.1 \times 10^{-2} - 3.0 \times 10^{-5}\mathrm{G}$	13.291	$+5.1 \times 10^{-2} - 3.1 \times 10^{-5}\mathrm{G}$	12.248	$+4.8 \times 10^{-2} + 1.2 \times 10^{-4}\mathrm{G}$
14	14.279	$-4.7 \times 10^{-2} + 2.4 \times 10^{-5}\mathrm{G}$	13.866	$-4.7 \times 10^{-2} + 2.5 \times 10^{-5}\mathrm{G}$	12.852	$-4.5 \times 10^{-2} - 8.3 \times 10^{-5}\mathrm{G}$
15	14.819	$+4.4 \times 10^{-2} - 1.9 \times 10^{-5}\mathrm{G}$	14.419	$+4.4 \times 10^{-2} - 2.0 \times 10^{-5}\mathrm{G}$	13.432	$+4.3 \times 10^{-2} + 5.7 \times 10^{-5}\mathrm{G}$
16	15.339	$-4.1 \times 10^{-2} + 1.6 \times 10^{-5}\mathrm{G}$	14.952	$-4.1 \times 10^{-2} + 1.6 \times 10^{-5}\mathrm{G}$	13.990	$-4.0 \times 10^{-2} - 4.0 \times 10^{-5}\mathrm{G}$
17	15.843	$+3.8 \times 10^{-2} - 1.3 \times 10^{-5}\mathrm{G}$	15.466	$+3.9 \times 10^{-2} - 1.4 \times 10^{-5}\mathrm{G}$	14.528	$+3.8 \times 10^{-2} + 2.9 \times 10^{-5}\mathrm{G}$
18	16.331	$-3.6 \times 10^{-2} + 1.1 \times 10^{-5}\mathrm{G}$	15.964	$-3.7 \times 10^{-2} + 1.2 \times 10^{-5}\mathrm{G}$	15.048	$-3.6 \times 10^{-2} - 2.1 \times 10^{-5}\mathrm{G}$
19	16.805	$+3.4 \times 10^{-2} - 9.5 \times 10^{-6}\mathrm{G}$	16.448	$+3.5 \times 10^{-2} - 9.8 \times 10^{-6}\mathrm{G}$	15.551	$+3.5 \times 10^{-2} + 1.5 \times 10^{-5}\mathrm{G}$
20	17.265	$-3.2 \times 10^{-2} + 8.1 \times 10^{-6}\mathrm{G}$	16.917	$-3.3 \times 10^{-2} + 8.5 \times 10^{-6}\mathrm{G}$	16.040	$-3.5 \times 10^{-2} - 1.2 \times 10^{-5}\mathrm{G}$

3.1. Heat Transfer Characteristics

The normalized bulk mean temperature, θ_m, can be defined as

$$\theta_m = \frac{T_m - T_s}{T_e - T_s} = \frac{1}{U_m A_c} \int_{A_c} U\theta \, dA = \frac{1}{U_m} \int_0^1 U\theta \, d\eta, \tag{36}$$

where T_m is the mean temperature and U_m is the mean velocity. From equations (12), (13), and (35) the normalized mean temperature can be found as

$$\theta_m = \frac{1}{U_m} G \left\{ \frac{1}{3} + \frac{4}{15}\Omega \right\} + \frac{1}{U_m} \sum_{n=1}^{\infty} A_n \exp\left[-\frac{\lambda_n^2}{\mathrm{Pe}_T} \xi \right] \int_0^1 U f_n \, d\eta. \tag{37}$$

Now from Fourier law of heat conduction, the wall heat flux can be obtained as

$$q_s'' = -\frac{k}{D}(T_e - T_s) \left(-G + \sum_{n=1}^{\infty} A_n \exp\left[-\frac{\lambda_n^2}{\mathrm{Pe}_T} \xi \right] \left. \frac{\partial f_n}{\partial \eta} \right|_{\eta=1} \right). \tag{38}$$

Also, from Newton's law of cooling, the heat flux can be expressed as

$$q_s'' = h_\xi (T_s - T_m), \tag{39}$$

where h_ξ is the local convective heat transfer coefficient. Therefore, from equations (38) and (39), the local heat transfer coefficient can be found as

$$h_\xi = \frac{q_s''}{T_s - T_m} = -\frac{k}{D}\frac{1}{\theta_m}\left.\frac{\partial \theta}{\partial \eta}\right|_{\eta=1} \tag{40}$$

and the corresponding Nusselt number, $\mathrm{Nu}_\xi = Dh_\xi/k$, for the mixed electroosmotic-pressure driven flow can be obtained as

$$\mathrm{Nu}_\xi = \frac{5\{3+2\Omega\}\left(G - \sum_{n=1}^{\infty} A_n \exp\left[-\left(\lambda_n^2/\mathrm{Pe}_T\right)\xi\right]\left.\frac{\partial f_n}{\partial \eta}\right|_{\eta=1}\right)}{G\{5+4\Omega\} + 15\sum_{n=1}^{\infty} A_n \exp\left[-\left(\lambda_n^2/\mathrm{Pe}_T\right)\xi\right]\int_0^1 \left\{1+\Omega\left(1-\eta^2\right)\right\} f_n \, d\eta}. \tag{41}$$

4. DISCUSSION OF RESULTS

For mixed electroosmotic and pressure-driven flows, the analytical solutions of heat transfer characteristics are obtained in equations (35), (37), (38), and (41). The eigenvalues and eigenfunctions used in this study are Sturm-Liouville nonself-adjoint operator, which are not orthogonal. Due to the nonexistence of the self-adjoint eigenvalues, we have presented our results in terms of Kummer confluent hypergeometric functions. The presence of special hypergeometric functions in eigenfunctions leads us to use numerical techniques to find the temperature distribution and related heat transfer characteristics. The convergence of the infinite series is very slow at $\xi = 0$, and hence we have plotted our results from $\xi = 0.01$.

In this study, the channel surface temperature is maintained at a fixed value, while the inlet temperature and electric fields are varied to obtain different value of G. Analytical solutions presented here are for $\mathrm{Re} < 1$ and $D \geq 1000\lambda$. Therefore the hydrodynamic entry length is negligible, and the mixed velocity distribution is justified from the very beginning of the channel. However, in solving the energy equation both thermally developing and fully developed regions are considered.

In this section, we plot the local fluid temperature (θ) and Nusselt number (Nu) distribution along the channel. We particularly present the thermally developing behavior at the entry region by considering Joule heating effects. Since Joule heating is a volumetric phenomenon, its effect is very significant in regular scale electrokinetic devices [21–23]. However in microchannel flows, the contributions of electric field and concentration cannot be underestimated. For typical electroosmotic microflows, the normalized Joule heating term (G) can vary between -1 to 1. Hence, we have presented the temperature distribution for only two different source term values ($G = -1$ and $G = +1$), though analytical solution obtained in this analysis can be used for any finite value of source term. Results presented in this section are a representative case for deionized water at $\mathrm{Re} \leq 0.7$, $\mathrm{Pr} = 7$, $\mathrm{Pe}_T \leq 5$. Due to the geometric, hydrodynamic, and thermal symmetry, the results are presented for only the upper half of the channel.

In Figure 4a, we illustrate the temperature distribution across the channel in pure electroosmotic flow for dimensionless source term $G = -1$. For the negative value of the source term, the channel surface temperature is higher than the inlet temperature of fluid ($T_s > T_e$). The normalized temperature becomes zero at the surface ($\eta = 1$) to conserve the isothermal boundary condition at the wall. At the entry the normalized temperature becomes unity across the channel. However, as the fluid travels along the channel, the fluid temperature, T, increases (θ and q_s'' decrease) due to volumetric Joule heating. Here, the wall heat flux reaches zero slightly after $\xi = 1$. Further down the channel, both normalized fluid temperature and wall heat flux become

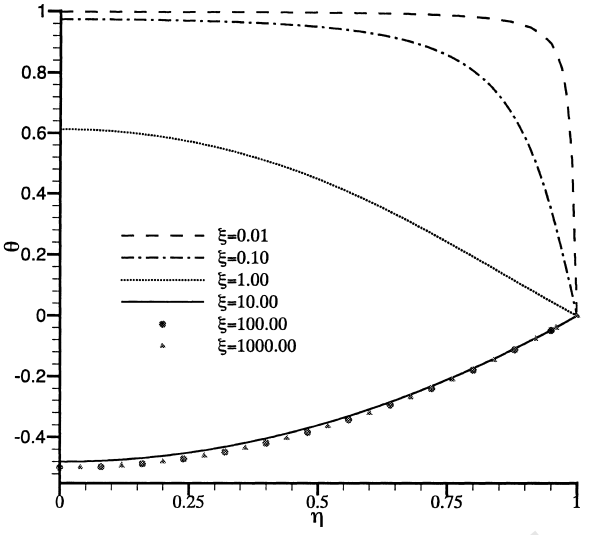

(a) $G = -1$.

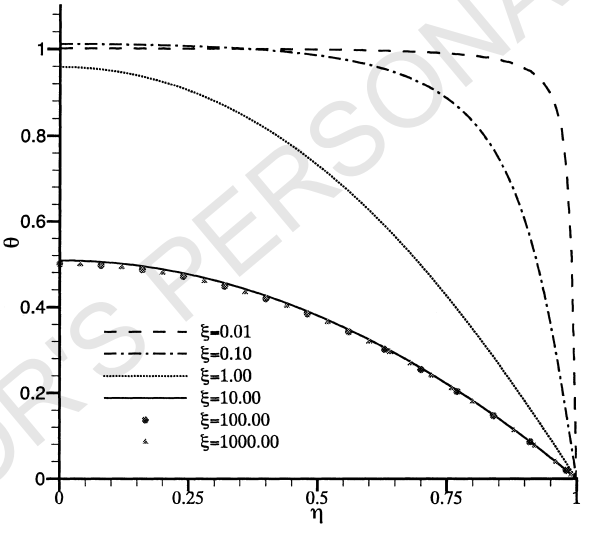

(b) $G = 1$.

Figure 4. Temperature distribution in pure electroosmotic flow at different longitudinal locations at $\mathrm{Pe}_T = 5$.

negative, and the temperature profile does not change anymore on or after $\xi = 10$. In this region, the thermal energy leaving through the boundary is equal to the heat generated by the Joule heating.

The normalized temperature distribution across the channel for the positive source term, $G = 1$, is presented in Figure 4b for pure electroosmotic flow. In this case, the fluid inlet temperature is higher than the channel surface temperature ($T_s < T_e$). Here both normalized and local fluid temperature decrease in the entry region, but they do not change after reaching $\xi = 10$. After that, the net energy transfer through the channel wall is equal to the volumetric thermal energy generation due to Joule heating. Unlike the negative source term ($G = -1$), the normalized temperature never falls below zero. Therefore, fluid temperature for this case is always higher than channel surface temperature and heat transfer always takes place from the fluid to the surroundings.

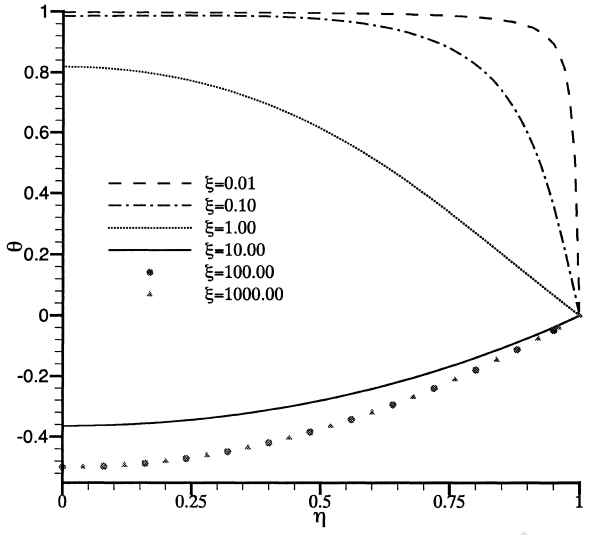

(a) $G = -1$.

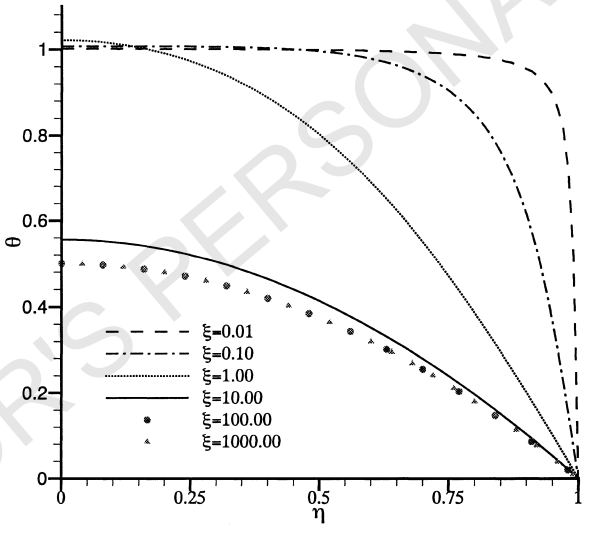

(b) $G = 1$.

Figure 5. Temperature distribution in mixed electroosmotic and pressure-driven flow for $\Omega = 1$ at different longitudinal locations at $\mathrm{Pe}_T = 5$.

The temperature distribution for the mixed electroosmotic and pressure-driven flows is presented in Figures 5 and 6 for normalized pressure gradient $\Omega = 1$ and 5, respectively. It is possible to find the temperature distribution for any value of $\Omega \geq -1.5$, although we have shown only two representative cases for positive Ω. The normalized pressure gradient indicates a ratio of pressure-driven velocity component at the channel centerline to Helmholtz-Smoluchowski velocity. Therefore, $\Omega = 1$ means the magnitude of pressure-driven velocity component at the centerline is same as the Helmholtz-Smoluchowski velocity. The positive value of the Ω provides favorable pressure gradient flow with net pressure drop along the channel. In case of positive Ω, the flow cannot be sustained only by the externally applied electric field.

Like pure electroosmotic flow, both positive and negative values of source terms ($G = -1$ and 1) are considered in this case. In the developing region the nondimensional temperature distribution follows the trends observed in the pure electroosmotic flow, while in the thermally

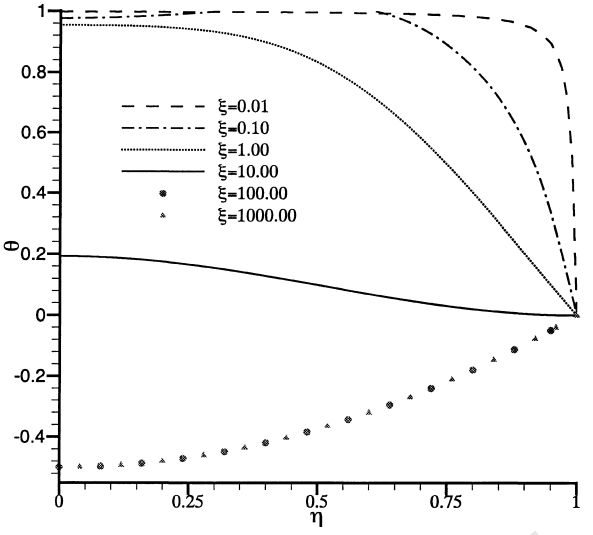

(a) $G = -1$.

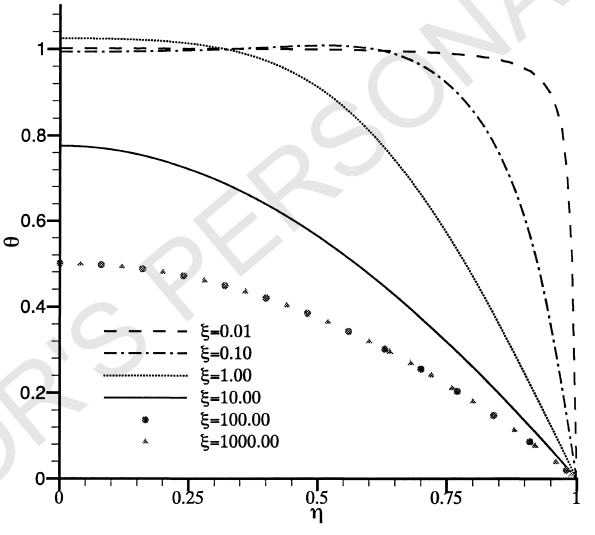

(b) $G = 1$.

Figure 6. Temperature distribution in mixed electroosmotic and pressure-driven flow for $\Omega = 5$ at different longitudinal locations at $\mathrm{Pe}_T = 5$.

fully developed region the normalized temperature distribution reaches to the identical values of pure electroosmotic flows for both $\Omega = 1$ and $\Omega = 5$ cases. However, the developing speed varies significantly with increase in the pressure gradient. For example, in mixed electroosmotic and pressure-driven flow, the temperature distribution across the channel changes until $\xi = 70$ for $\Omega = 5$, as opposed to until $\xi = 10$ in the pure electroosmotic flows. The longer thermal entrance length at the favorable pressure gradient flow is mainly due to the higher flow velocity of the fluid.

Figure 7 shows the normalized temperature distribution across the channel for $\Omega = -1$. The negative Ω value corresponds to adverse pressure gradient flow where there is a net gain in the pressure head. This net pressure gain could be used to drive the microflow in the electroosmotically suppressed region [5]. Moreover, in the absence of any external forcing mechanism, the adverse pressure gradient case is used to compensate any pressure drop in the corners and turns.

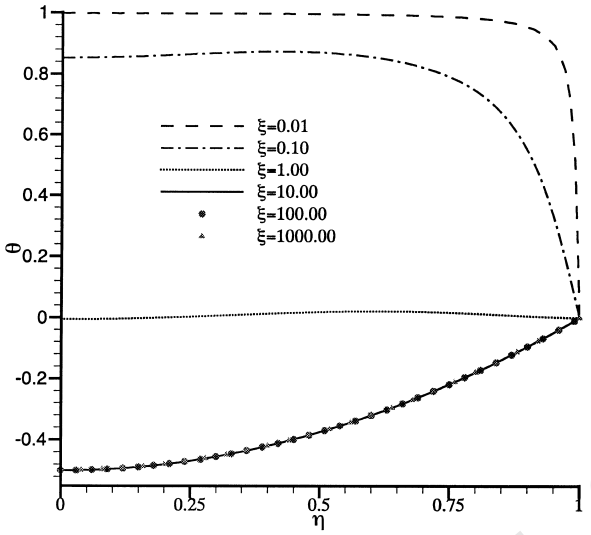

(a) $G = -1$.

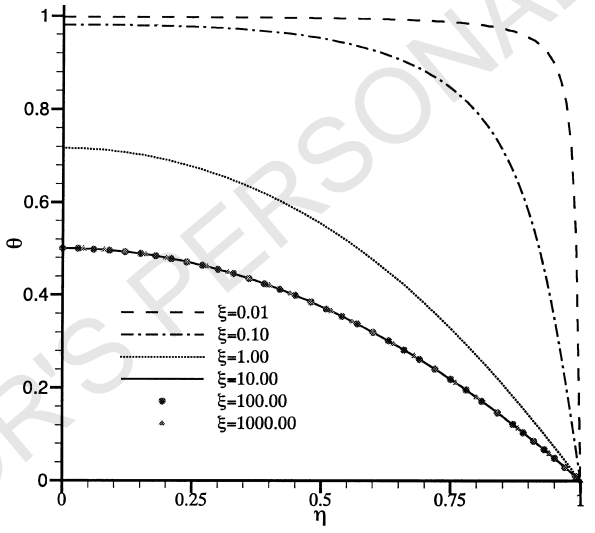

(b) $G = 1$.

Figure 7. Temperature distribution in mixed electroosmotic and pressure-driven flow for $\Omega = -1$ at different longitudinal locations at $\mathrm{Pe}_T = 5$.

Even though adverse pressure gradient flow provides net pressure head in the microfluidic systems for additional pumping, the net discharge is less than corresponding pure electroosmotic case. As for example, for $\Omega = -1$, the discharge is only 33% of the pure electroosmotic flow. In this case, the thermally fully developed region can be obtained much faster than pure electroosmotic flow for both positive and negative values of G.

In all four cases presented above, the fully developed temperature at any lateral location is the same for a particular value of $|G|$ (provided σ, $\vec{E}$, k, and D are constant), although their corresponding nondimensional magnitude depends on the sign of the normalized source term. As for example, from Figures 4–7, the normalized centerline temperature in the fully developed region becomes $\theta_{c,fd} \rightarrow G/2$. However, the fully developed dimensional temperature at the channel centerline can be obtained as $T_c = T_s + 0.5|T_e - T_s||G|$. Therefore, the fully developed dimensional temperature is maximum at the channel centerline and minimum at the channel surface.

Figure 8 shows the local Nusselt number distribution along the channel for all four cases ($\Omega = 0$, 1, 5, and -1) presented in Figures 4–7 for normalized source term $G = -1$ and 1. Due to the identical nature of the local Nusselt number after reaching the fully developed condition, they have been presented until $\xi = 100$. For isothermal channel surface condition, the Nusselt number is very high at the entry point. But it decays quickly to reach a flat value within one characteristic length (D). The rationale for this abrupt decay is that the thermal boundary layer develops along the flow direction. The spike in the local Nusselt number distribution for $G = -1$ shows the location along the channel where the mean temperature approaches the surface temperature. In case of negative generation term ($G < 0$), the fluid temperature (T) increases due to both Joule heating and surface thermal condition until it exceeds the surface temperature. After that the temperature rise is due to the Joule heating only, and the maximum temperature attained by the fluid is higher than the channel surface temperature ($T_{\max} > T_s > T_e$). Figure 8

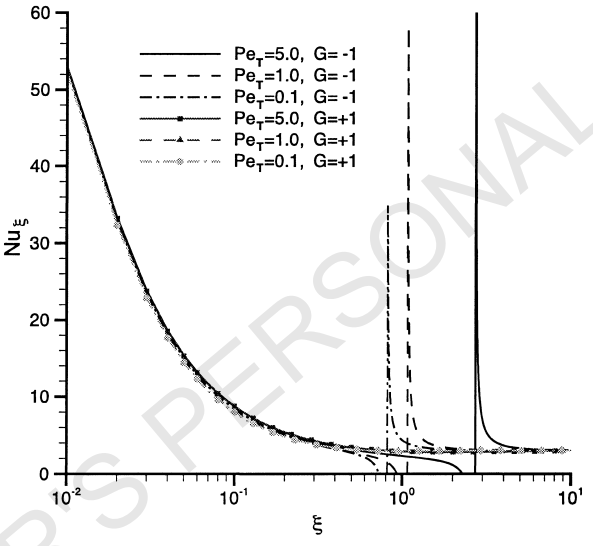

(a) $\Omega = 0$.

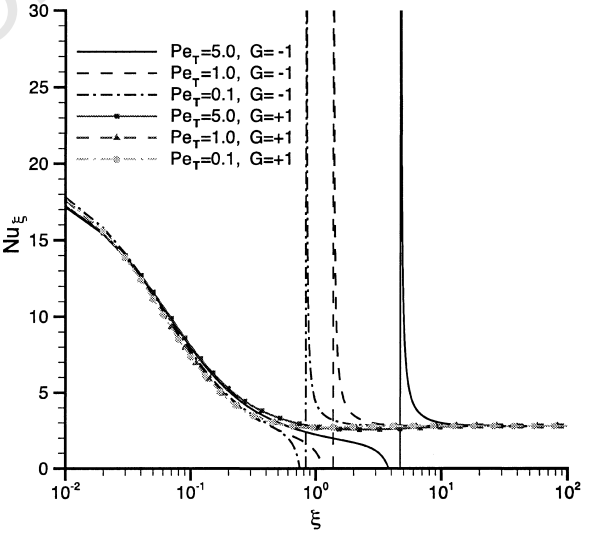

(b) $\Omega = 1$.

Figure 8. Local Nusselt number distribution along the channel for different Joule heating value at different Peclet numbers.

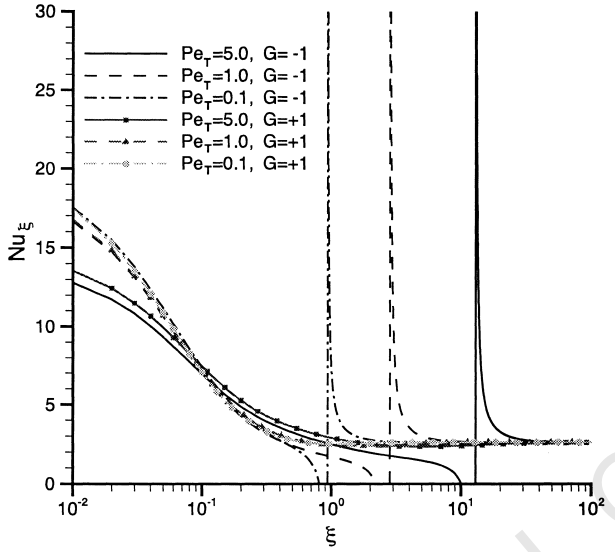

(c) $\Omega = 5$.

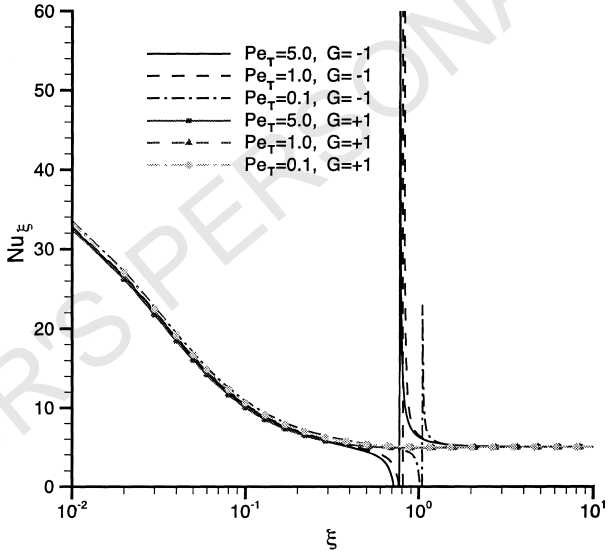

(d) $\Omega = -1$.

Figure 8. (Cont.)

Table 2. Comparison of Nusselt number (Nu_{D_H}) in the fully developed region for low Peclet number ($\mathrm{Pe}_T \leq 5$) flow with the existing literature.

	$G = -1$		$G = 0$		$G = +1$	
	This Study	Reference	This Study	Reference	This Study	Reference
Mixed Flow ($\Omega = -1.0$)	20.00	–	18.90	–	20.00	–
Electroosmotic Flow	12.00	12.00 [18]	9.87	9.87 [24]	12.00	12.00 [18]
Mixed Flow ($\Omega = +1.0$)	11.11	–	8.80	–	11.11	–
Mixed Flow ($\Omega = +5.0$)	10.40	–	7.98	–	10.40	–
Poiseuille flow	10.00	–	7.59	7.59 [13]	10.00	–

location of fully (thermally) developed regions. From the local temperature and Nusselt number distribution, it is clear that the thermally developing region is shorter for positive generation term ($T_e > T_s$) than that of negative generation term.

For each case, we also studied the dependence of thermal Peclet number. For a particular flow, the fully developed Nusselt number is independent of the Peclet number, and it does not depend on the magnitude of the source term, except for the no generation case ($G = 0$). If there is no Joule heating the heat transfer behaviors will be significantly different from those presented in Figures 4–7, though our analytical results can still be used for no Joule heating cases. The fully developed Nusselt numbers for different source term values are presented in Table 2. Here, our Nusselt number values are computed based on hydraulic diameter ($\mathrm{Nu}_{D_H} = 4\,\mathrm{Nu}_D$). For both positive and negative source terms considered in this study ($G = 1$ and -1), in pure electroosmotic flow, the Nusselt number reaches a value of 12.0 in the fully developed region. For cases without Joule heating, the heat transfer characteristics of pure electroosmotic flow are identical to the classical isothermal heat transfer in a slug flow, for which the fully developed Nusselt number is 9.868 [24]. In the fully developed region, the Nusselt number for the electroosmotic flow is significantly higher than that of Poiseuille flow. The higher heat transfer characteristics in pure electroosmotic flow can be attributed to the plug-like uniform velocity. In pure electroosmotic and Poiseuille flows, the fully developed Nusselt numbers are also compared with the existing literatures (in Table 2) for identical geometric, electrokinetic, and thermal conditions. In the fully developed region our analytical results exactly match with the other existing studies.

The fully developed Nusselt number in mixed electroosmotic-pressure driven flow decreases as normalized pressure gradient increases. Note that the heat flux at the wall is the same for all cases in the fully developed region, and it can be explained from temperature distribution in Figures 4–7. This implies that the normalized bulk mean temperature gets bigger as the pressure gradient increases, which solely depends on the normalized velocity distribution across the channel. The normalized bulk mean temperature has the highest value when the fluid is driven by favorable pressure gradient with $\Omega \to \infty$. This case is identical to Poiseuille flow, for which the fully developed Nusselt number is 7.59. On the other hand, the normalized bulk mean temperature reaches its minimum value for adverse pressure gradient flow ($\Omega \to -1.5$).

5. CONCLUSIONS

We obtained analytical solutions for heat transfer characteristics of mixed electroosmotic-pressure driven flows in two-dimensional straight microchannels for constant zeta potential, buffer concentration, and external electric field. This analysis takes care of interaction among advective, viscous, and Joule heating terms to obtain the temperature distribution within the fluid. Our analysis resulted in the following.

1. For an isothermal channel surface condition, the local fluid temperature decreases for a positive source term ($G > 0$) and increases for a negative source term ($G < 0$) along the channel, before it reaches an identical profile.
2. For a particular flow type (in the fully developed region), the normalized heat transfer coefficient reaches the same value for both positive and negative source terms.
3. The heat transfer coefficient of mixed electroosmotic and pressure-driven flow is smaller than that of pure electroosmotic flow for favorable pressure gradient case.
4. Electroosmotic flow with adverse pressure gradient provides the best heat transfer performance.
5. The temperature profile in the fully developed region is independent of Peclet number and pressure gradient.
6. In the mixed electroosmotic-pressure driven flows, the thermal entrance length increases with the imposed pressure gradient.

APPENDIX A

GRAM-SCHMIDT ORTHOGONAL PROCEDURE

Let us assume a series of orthogonal function, g_i, which are related to our eigenfunctions as

$$g_1 = f_1, \tag{A.1}$$

$$g_2 = f_2 - \alpha_{21} f_1, \tag{A.2}$$

$$g_3 = f_3 - \alpha_{31} f_1 - \alpha_{32} f_2, \tag{A.3}$$

$$\vdots$$

$$g_i = f_i - \sum_{j=1;\, i \geq 2}^{i-1} \alpha_{ij} f_j, \tag{A.4}$$

where α_{ij} are constants. Our next step is to obtain these constants in order to find orthogonal functions g_i. From the property of orthogonal function, we can write following relationship:

$$\int_0^1 g_i \cdot g_j \, d\eta = 0, \tag{A.5}$$

if $i \neq j$ for $i = 1, 2 \ldots$ and $j = 1, 2 \ldots$.

Now by multiplying equation (A.2) with g_1 and integrating over the domain $(0 \leq \eta \leq 1)$, we get

$$\int_0^1 g_2 \cdot g_1 \, d\eta = \int_0^1 f_2 \cdot f_1 \, d\eta - \alpha_{21} \int_0^1 f_1 \cdot f_1 \, d\eta = 0. \tag{A.6}$$

From the above equation, we can find an expression for α_{21} as

$$\alpha_{21} = \frac{\int_0^1 f_2 \cdot f_1 \, d\eta}{\int_0^1 f_1^2 \, d\eta} = \frac{\langle f_2, f_1 \rangle}{\|f_1\|^2}, \tag{A.7}$$

where $\|\cdot\|$ represents the norm of $L^2(0,1)$ space. Similarly, we can find each α_{ij} by

$$\alpha_{ij} = \frac{\langle f_i, f_j \rangle}{\|f_j\|^2}. \tag{A.8}$$

Now we expand the homogeneous part of the nondimensional temperature, θ_g, at the inlet boundary $(\xi = 0)$ as a series of $\{g_n\}$.

$$\theta_g|_{\xi=0} = 1 - \frac{G}{2}\left(1 - \eta^2\right) = \sum_{n=1}^{\infty} B_n g_n. \tag{A.9}$$

It follows that

$$B_n = \frac{\int_0^1 \left\{1 - (G/2)\left(1 - \eta^2\right)\right\} g_n \, d\eta}{\int_0^1 g_n^2 \, d\eta}, \tag{A.10}$$

for $n = 1, 2 \ldots$.

Finally the original coefficients A_n can be found by recalling the definition of g_i, from equations (A.1)–(A.4), as

$$\begin{aligned}\sum_{n=1}^{N} B_n g_n &= B_1 g_1 + B_2 g_2 + B_3 g_3 + \cdots + B_i g_i + \cdots + B_N g_N \\ &= B_1(f_1) + B_2(f_2 - \alpha_{21} f_1) + \cdots B_i \left(f_i - \sum_{j=1;\, i\geq 2}^{i-1} \alpha_{ij} f_j \right) \\ &\quad + \cdots + B_N \left(f_N - \sum_{j=1}^{N-1} \alpha_{Nj} f_j \right) \\ &= \left(B_1 - \sum_{j=2}^{N} \alpha_{j1} B_j \right) f_1 + \cdots \left(B_i - \sum_{j=i+1}^{N} \alpha_{ji} B_j \right) f_i + \cdots + B_N f_N \\ &= A_1 f_1 + A_2 f_2 + A_3 f_3 + \cdots + A_i f_i + \cdots + A_N f_N \\ &= \sum_{n=1}^{N} A_n f_n,\end{aligned} \tag{A.11}$$

where N is a sufficiently large number to represent infinity. Therefore, coefficients A_i become

$$A_1 = B_1 - \sum_{j=2}^{N} \alpha_{j1} B_j = B_1 - \sum_{j=2}^{N} \frac{\langle f_j, f_1 \rangle}{\|f_1\|^2} B_j, \tag{A.12}$$

$$A_i = B_i - \sum_{j=i+1}^{N} \alpha_{ji} B_j = B_i - \sum_{j=i+1}^{N} \frac{\langle f_j, f_i \rangle}{\|f_i\|^2} B_j, \tag{A.13}$$

$$\vdots$$

$$A_N = B_N. \tag{A.14}$$

REFERENCES

1. A. Richter, A. Plettner, K.A. Hofmann and H. Sandmaier, A micromachined electrohydrodynamic (EHD) pump, *Sensors and Actuators A* **29**, 159–168, (1991).
2. J. Jang and S.S. Lee, Theoretical and experimental study of MHD (magnetohydrodynamic) micropump, *Sensors and Actuators A* **80**, 84–89, (2000).
3. C.H. Chen and J.G. Santiago, A planar electroosmotic micropump, *J. Micro-Electromechanical Systems* **11** (6), 672–683, (2002).
4. D. Burgreen and F.R. Nakache, Electrokinetic flow in ultrafine capillary silts, *J. Physical Chemistry* **68** (5), 1084–1091, (1964).
5. P. Dutta and A. Beskok, Analytical solution of combined electroosmotic/pressure driven flows in two-dimensional straight channels: Finite Debye layer effects, *Analytical Chemistry* **73**, 1979–1986, (2001).
6. O. Soderman and B. Jonsson, Electro-osmosis: Velocity profiles in different geometries with both temporal and spatial resolution, *J. of Chem. Phys.* **105**, 10300–10311, (1996).
7. P. Dutta and A. Beskok, Analytical solution of time periodic electroosmotic flows: Analogies to Stokes' second problem, *Analytical Chemistry* **73**, 5097–5102, (2001).
8. P.K. Wong, C.Y. Chen, T.H. Wang and C.M. Ho, An AC electroosmotic processor for biomolecules, *Proc. of 12th International Conference on Solid State Sensors, Actuators and Microsystems* **1A3.2**, 20–23, (2003).
9. S. Zeng, C.H. Chen, J.C. Mikkelsen and J.G. Santiago, Fabrication and characterization of electroosmotic micropumps, *Sensors and Actuators B* **79**, 107–114, (2001).
10. D. Maynes and B.W. Webb, Fully-developed thermal transport in combined pressure and electro-osmotically driven flow in microchannels, *ASME J. Heat Transfer* **125**, 889–895, (2003).
11. E.M. Sparrow, J.L. Novotny and S.H. Lin, Laminar flow of a heat-generating fluid in a parallel-plate channel, *A.I.Ch.E. Journal* **9** (6), 797–804, (1963).
12. H.C. Agrawal, Heat transfer in laminar flow between parallel plates at small Peclet number, *Appl. Sci. Res. A* **9**, 177–189, (1960).
13. J. Lahjomri and A. Oubarra, Analytical solution of the Graetz problem with axial conduction, *ASME J. Heat Transfer* **121**, 1078–1083, (1999).

14. R.J. Hunter, *Zeta Potential in Colloid Science: Principles and Applications*, First Edition, Academic Press, New York, (1981).
15. R.F. Probstein, *Physicochemical Hydrodynamics*, Second edition, Wiley and Sons, New York, (1994).
16. P. Dutta, A. Beskok and T.C. Warburton, Numerical simulation of mixed electroosmotic/pressure driven microflows, *Numerical Heat Transfer, Part A* **41**, 131–148, (2002).
17. O.L. Sanchez Munoz, E. Perez Hernandez, M. Lammerhofer, W. Lindner and E. Kenndler, Estimation and comparison of ζ-potentials of silica-based anion-exchange type porous particles for capillary electrochromatography from electrophoretic and electroosmotic mobility, *Electrophoresis* **24**, 390–398, (2003).
18. K. Horiuchi and P. Dutta, Joule heating effects in electroosmotically driven microchannel flows, *Int. J. Heat and Mass Transfer* **47**, 3085–3095, (2004).
19. M. Abramowitz and I.A. Stegun, Editors, *Handbook of Mathematical Functions with Formulas, Graphs, and Mathematical Tables*, Ninth Edition, Dover, New York, (1972).
20. G. Arfken, *Mathematical Methods for Physicists*, Third Edition, Academic Press, Florida, (1985).
21. W.A. Gobie and C.F. Ivory, Thermal model of capillary electrophoresis and a method of counteracting thermal band broadening, *J. Chromatography* **516**, 191–210, (1990).
22. D.S. Burgi, K. Salomon and R.L. Chien, Methods for calculation the internal temperature of capillary columns during capillary electrophoresis, *J. Liquid Chromatography* **14**, 847–867, (1991).
23. K. Swinney and D.J. Bornhop, Quantification and evaluation of Joule heating in on-chip capillary electrophoresis, *Electrophoresis* **23**, 613–620, (2002).
24. L.C. Burmeister, *Convective Heat Transfer*, Second Edition, Wiley and Sons, New York, (1993).